




# Adsorption characteristics of copper ion on nanoporous silica

Yanhui Niu<sup>1,2,3</sup> · Wenbin Yu<sup>1</sup> · Zonghua Qin<sup>1</sup> · Xin Nie<sup>1</sup> · Shuguang Yang<sup>1,2</sup> ·  
Quan Wan<sup>1,2,4</sup> 

Received: 26 March 2019 / Revised: 10 May 2019 / Accepted: 4 June 2019 / Published online: 12 June 2019  
© Science Press and Institute of Geochemistry, CAS and Springer-Verlag GmbH Germany, part of Springer Nature 2019

**Abstract** Adsorption by nanoporous media is critically involved in many fundamental geological and geochemical processes including chemical weathering, element migration and enrichment, environmental pollution, etc. Yet, the adsorption behavior of metal ions on nanoporous materials has not been systematically investigated. In this study, MCM-41 material with a monodisperse pore size (4.4 nm) and a large BET specific surface area (839 m<sup>2</sup>/g) was hydrothermally prepared and used as a model silica adsorbent to study the adsorption characteristics of Cu<sup>2+</sup> as a representative metal ion. The Cu<sup>2+</sup> adsorption capacity was found to increase with increasing suspension pH in the range from 3 to 5 and to decrease in the presence of NaNO<sub>3</sub>. At 25 °C, pH = 5, and a solid-to-liquid ratio of 5 g/L, the adsorption capacity was determined to be 0.29 mg/g, which can be converted to a dimensionless partition coefficient of 45, indicating a strong enriching effect of nanoporous silica. The adsorption isotherm and kinetic data were fitted to several commonly used thermodynamic, kinetic, and diffusion models. The adsorption mechanism was also studied by Fourier transform infrared

spectroscopy, X-ray photoelectron spectroscopy and synchrotron-based X-ray absorption spectroscopy. The results suggest that Cu<sup>2+</sup> ion adsorption is an entropy-driven endothermic process, possibly involving both outer-sphere and inner-sphere complexes.

**Keywords** Nanoporous silica · Copper ion · Adsorption

## 1 Introduction

Nanoporous materials are well known for their much larger specific surface area and distinctive reactivities compared with nonporous materials (Wang et al. 2002). It has also been recognized that the properties of fluids in nanopores can differ very much from those of bulk fluids, indicating the prominent effect of nano-confinement. As an example, the freezing point, dielectric constant and even density of water in nanopores can be significantly lower than those of bulk water (Jahnert et al. 2008; Senapati and Chandra 2001; Takei et al. 2000). These unique features make synthetic nanoporous materials excellent candidates in numerous applications, such as catalysis (Ben Said et al. 2018; Hu et al. 2018; Taguchi and Schuth 2005), electrochemistry (Xu et al. 2003), adsorption (Dou et al. 2011), separation (Lam et al. 2007; Ravi et al. 2015) and so on. Interestingly, naturally occurring nanopores have been commonly found in various geological media including rocks, soils, sediments, minerals, organisms, etc., and may tremendously contribute to the total surface areas (Wang et al. 2003). Furthermore, it has become a consensus that these widespread nanopores play substantial roles in many important geoscience issues such as chemical weathering (Hochella 2013; Hochella and Banfield 1995; Hochella et al. 2008), element migration and enrichment (Cheng

✉ Quan Wan  
wanquan@vip.gyg.ac.cn

<sup>1</sup> State Key Laboratory of Ore Deposit Geochemistry, Institute of Geochemistry, Chinese Academy of Sciences, 99 Lincheng West Road, Guanshanhu District, Guiyang 550081, Guizhou, China  
<sup>2</sup> University of Chinese Academy of Sciences, Beijing 100049, China  
<sup>3</sup> School of Chemistry and Materials Science, Guizhou Education University, 115 Gaoxin Road, Wudang District, Guiyang 550018, Guizhou, China  
<sup>4</sup> CAS Center for Excellence in Comparative Planetology, Hefei 230026, Anhui, China

et al. 2012), treatment of environmental pollutants, storage and transport of unconventional oil and gas (Bernard et al. 2012; Gu et al. 2018; Loucks et al. 2009; Oliver et al. 1995), geological storage of carbon dioxide (Rother et al. 2012), organic matter preservation (Zimmerman et al. 2004), etc. While adsorption of nanoporous media has been considered a key process in many aforementioned fields, many previous studies either aiming at enhancing adsorption efficiency through surface modification of nanopores or using natural nanoporous samples with inevitable compositional and structural complexity are not conducive to a clear understanding of the adsorption mechanism (Bradl 2004; Chen et al. 2017; Huang et al. 2012; Matsumoto et al. 2002; Schulthess et al. 2011; Yuan et al. 2008). Up to now, there is still a lack of systematic investigations on the adsorption behavior of nanoporous materials.

Recently, synthetic nanoporous silica materials began to attract considerable attention from geoscientists as model materials in adsorption studies, because silica represents one of the most abundant components of the Earth's crust and synthetic samples usually exhibit controllable composition and structure (Knight et al. 2018; Radha et al. 2016; Singer et al. 2014; Wu et al. 2014; Wu and Navrotsky 2013). Among those nanoporous silicas, SBA-15 and MCM-41 type mesoporous (pore size: 2–50 nm) silicas have caught special interest due to their large specific surface area, well-controlled size, and ordered pore arrangement. However, in addition to mesopores, SBA-15 silica normally contains a large number of micropores (pore size < 2 nm) (Gibson 2014), which may bring sometimes overlooked complication to the adsorption process (Schulthess et al. 2011). For MCM-41 silica, although having monodispersed mesopores without any micropores, previous research still focused more on efficient adsorption of contaminants (e.g., heavy metal ions) by surface modification of nanopores (Elo et al. 2017; Faghihian and Naghavi 2014; Guo et al. 2015; He et al. 2018; Lee et al. 2016; Zhang et al. 2018). After modification, the geometry, volume, and surface functional groups of the nanopores can be substantially changed, and accordingly, the observed adsorption behavior cannot truly reflect the characteristics of natural nanopores. To our knowledge, only a very limited number of studies explored the adsorption behavior of unmodified MCM-41 silica (Thirumavalavan et al. 2011; Tian et al. 2011).

Therefore, we were motivated to systematically determine the adsorption properties of unmodified MCM-41 nanoporous silica using copper ion ( $\text{Cu}^{2+}$ ) as a representative adsorptive. Besides the routine uptake experiments, we also carried out thermodynamic, kinetic, and spectroscopic analyses to investigate the adsorption mechanism of  $\text{Cu}^{2+}$  on MCM-41. Our work would provide useful insights

for a better understanding of the complex roles of geological nanoporous media.

## 2 Experiments

### 2.1 Materials

Tetraethyl orthosilicate (TEOS, 99%), octadecyltrimethyl ammonium bromide (OTAB, 99%) and ammonia (25–28 wt %) were purchased from Aladdin (Shanghai, China). Copper nitrate [ $\text{Cu}(\text{NO}_3)_2 \cdot 3\text{H}_2\text{O}$ , 99%] was obtained from West Long Co., Ltd. (Guangzhou, China). All chemical reagents in this study were used without further purification. Deionized water was obtained from a Millipore synergy UV system (Millipore corporation, Molsheim, Alsace, France) and had a resistivity of 18.2  $\text{M}\Omega\text{-cm}$ .

MCM-41 silica was prepared according to a procedure by Grün M et al (Grun et al. 1999), in which a synthesis mixture with a molar ratio of 1TEOS:0.152OTAB:2.8 $\text{NH}_3 \cdot \text{H}_2\text{O}$ :141.2 $\text{H}_2\text{O}$  was hydrothermally treated at 105 °C for 18 days. In a typical synthesis, 8.31 g of OTAB as the template was first dissolved in 381 g of deionized water. After the solution became clear, 28.50 g of ammonia was added to the above solution. Then, 31.25 g of TEOS was added slowly to the solution over a period of 20 min under stirring. After the hydrothermal treatment, the solid sample was obtained through filtration, washed with copious water, and dried at room temperature. Subsequently, the sample was heated up from room temperature to 550 °C at a heating rate of 1 °C / min, and calcined at 550 °C in air for 6 h to produce the nanoporous MCM-41 silica.

### 2.2 Characterization methods

The adsorption and desorption isotherms of  $\text{N}_2$  were obtained at  $-196$  °C using a gas adsorption analyzer (Autosorb-iQ<sub>2</sub>-MP, Quantachrome). The samples were degassed at 200 °C under vacuum for 20 h before measurement. The BET (Brunauer–Emmett–Teller) model was used to analyze the specific surface area and the NLDFT (nonlocal density functional theory) model was used to analyze the pore size and pore volume.

The morphology and structure of the samples were characterized using a transmission electron microscope (TEM; FEI Tecnai G2F20 S-TWIN TMP) operated at 200 kV and a scanning electron microscope (SEM, FEI, USA) scanned at 1 kV.

X-ray diffraction (XRD) was performed on a PANalytical EMPYREAN instrument equipped with  $\text{Cu K}\alpha$  radiation ( $\lambda = 1.5418$  Å) using an operating voltage of 40 kV and an operating current of 40 mA. XRD measurements

were conducted over a  $2\theta$  range from  $0.5$  to  $10^\circ$  with a step size of  $0.013^\circ$  and a scanning speed of  $0.034^\circ/\text{min}$ .

Attenuated total reflectance infrared (ATR-IR) spectra were recorded over a range of  $1200$ – $600\text{ cm}^{-1}$  with an accumulation of 256 scans and a spectral resolution of  $2\text{ cm}^{-1}$  using a Bruker Vertex 70 spectrometer equipped with a mercury cadmium telluride (MCT) detector.

Differential scanning calorimetry measurements were conducted over a temperature range from  $-83$  to  $7^\circ\text{C}$  at a heating rate of  $0.5^\circ\text{C}/\text{min}$  using a Discovery DSC 250 (TA Instruments, America). An air-dried MCM-41 sample ( $2.3\text{ mg}$ ) was put into an aluminum pan and contacted with an excess of water (up to  $10\text{ mg}$ ). The pan was then sealed and reweighed.

The point of zero charge (PZC) of MCM-41 was obtained with an automatic potentiometric titrator (Metrohm 905, Switzerland). A suspension was prepared by mixing the MCM-41 powder with water at  $25^\circ\text{C}$  in a constant-temperature oscillator for 24 h (consistent with the time of adsorption experiment). The suspension was first titrated to  $\text{pH} = 1.6$  with  $5\%$   $\text{HNO}_3$  and then back-titrated to  $8.0$  with  $0.5\text{ M NaOH}$ . The blank solution was obtained by filtering the suspension through a  $0.45\text{ }\mu\text{m}$  membrane filter. The PZC was determined as the  $\text{pH}$  value at the intersection point of the titration curves of the blank solution and the suspension.

X-ray photoelectron spectroscopy (XPS) data were collected on an ESCALAB 250Xi spectrometer (ThermoFisher scientific, America) using an  $\text{Al K}\alpha$  radiation ( $1486.6\text{ eV}$ ). The  $\text{Al K}\alpha$  source was operated at  $15\text{ kV}$  and  $10\text{ mA}$ . The binding energy values were charge-corrected to the  $\text{C1s}$  signal ( $284.8\text{ eV}$ ).

Cu L-edge XANES spectroscopy analyses were carried out at 4B7B beam-line using synchrotron radiation from Beijing Synchrotron Radiation Facility, Institute of High Energy Physics of China. Cu L-edge XANES spectra data were recorded in the total electron yield (TEY) mode with an energy step of  $0.2\text{ eV}$  from  $915$  to  $960\text{ eV}$ .

### 2.3 Batch sorption experiment

All batch sorption experiments were carried out in  $25\text{ mL}$  flasks. A  $\text{Cu}^{2+}$  stock solution was prepared by dissolving  $\text{Cu}(\text{NO}_3)_2 \cdot 3\text{H}_2\text{O}$  in distilled water. About  $10\text{ mL}$  of an aqueous solution containing  $2$ ,  $4$ ,  $6$ ,  $8$ , and  $10\text{ mg/L}$  of  $\text{Cu}^{2+}$  was added to the  $25\text{ mL}$  glass flask and shaken with  $0.05\text{ g}$  of MCM-41 nanoporous silica in a constant-temperature oscillator (ZWYR-D2304, LABWIT Scientific, China) for a period of time ranging from  $1$  to  $36\text{ h}$ . Adsorption experiment was carried out at a temperature of  $5$  and  $25^\circ\text{C}$ . The solution  $\text{pH}$  was adjusted by adding drops of  $0.1\text{ M HNO}_3$  and  $\text{NaOH}$  for all experiments. Suspensions were then filtered using a  $0.45\text{ }\mu\text{m}$  PVDF syringe

filter and the  $\text{Cu}^{2+}$  concentrations of the supernatants were determined by atomic absorption spectrometry (AAS, 990SUPER, Beijing Purkinje General Instrument Co., Ltd., China).  $Q_e$  ( $\text{mg/g}$ ), the amount of  $\text{Cu}^{2+}$  adsorbed per unit mass of the adsorbent was calculated by the following equation:

$$Q_e = \frac{(C_0 - C_e)V}{W} \quad (1)$$

where  $C_0$  is the concentration of  $\text{Cu}^{2+}$  in the initial solution ( $\text{mg/L}$ ),  $C_e$  is the equilibrium concentration of  $\text{Cu}^{2+}$  in the aqueous phase ( $\text{mg/L}$ ),  $V$  is the volume of the aqueous phase ( $\text{L}$ ), and  $W$  is the dry weight of the adsorbent ( $\text{g}$ ).

## 3 Results and discussion

### 3.1 Characterization of the MCM-41 nanoporous silica

The low-angle X-ray diffraction pattern of our MCM-41 sample shows a high-intensity peak (corresponding to a  $d$ -spacing of  $4.48\text{ nm}$ ) and four higher-angle peaks between  $0.5$  and  $10.0^\circ$  (Fig. 1a), which can be indexed as (100), (110), (200), (210), and (300) reflections of the two-dimensional hexagonal structure, respectively (Beck et al. 1992). The relatively narrow width of the (100) peak along with the appearance of four additional diffraction peaks indicates high-quality ordering of our sample (Huo et al. 1996; Kruk et al. 1997). While the SEM image (Fig. 1b) shows the slightly curled, short rod-like ( $0.3 \times 1.2\text{ }\mu\text{m}$ ) morphology of our MCM-41 silica, TEM (Fig. 1c) presents highly regular arrays of uniform nano-sized channels in accordance with the well-defined 2-d hexagonal phase. The ATR-IR study (Fig. 1d) reveals that the peaks at  $1479$ ,  $2853$ , and  $2923\text{ cm}^{-1}$  characteristic of OTAB (Costa et al. 2014) disappear in the spectrum of the calcined sample, suggesting efficient removal of organic template through calcination ( $550^\circ\text{C}$ ,  $6\text{ h}$ ).

The  $\text{N}_2$  adsorption/desorption isotherm of the MCM-41 silica (Fig. 2a) is identified as type IV and exhibits capillary condensation with a narrow Type I hysteresis loop as reported in previous studies (Schreiber et al. 2001). These features are considered signature evidence of mesoporosity with relatively narrow pore size distribution (Thommes et al. 2015), consistent with the calculated NLDFT results shown in Fig. 2b. The average pore size of MCM-41 by NLDFT was found to be  $4.4\text{ nm}$ , in rough agreement with the estimation by TEM. The nanopore volume by NLDFT was  $0.9\text{ cm}^3/\text{g}$ , and the BET specific surface area of MCM-41 was  $839\text{ m}^2/\text{g}$ .

The above characteristics including simple silica composition, high-quality ordering, nearly monodispersed

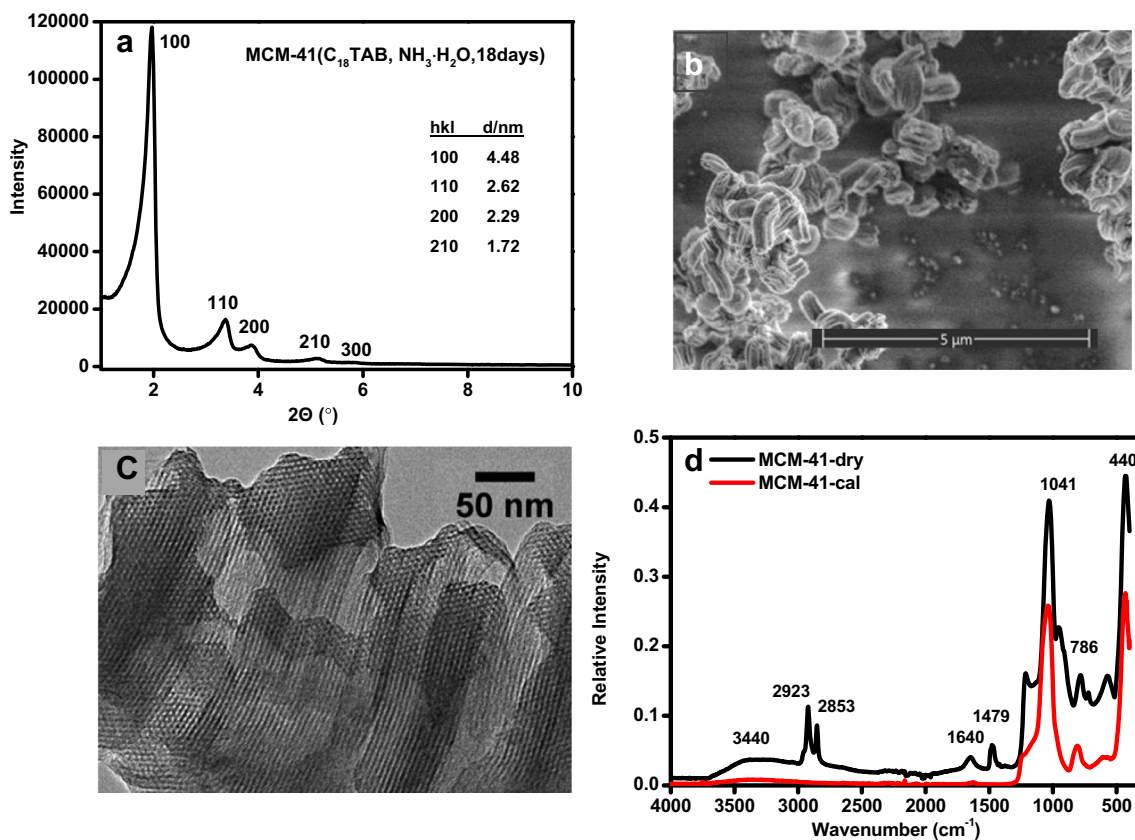


**Fig. 1** **a** XRD, **b** SEM, **c** TEM, and **d** ATR-IR characterization of MCM-41 silica, MCM-41-dry/MCM-41-cal: sample before or after calcination

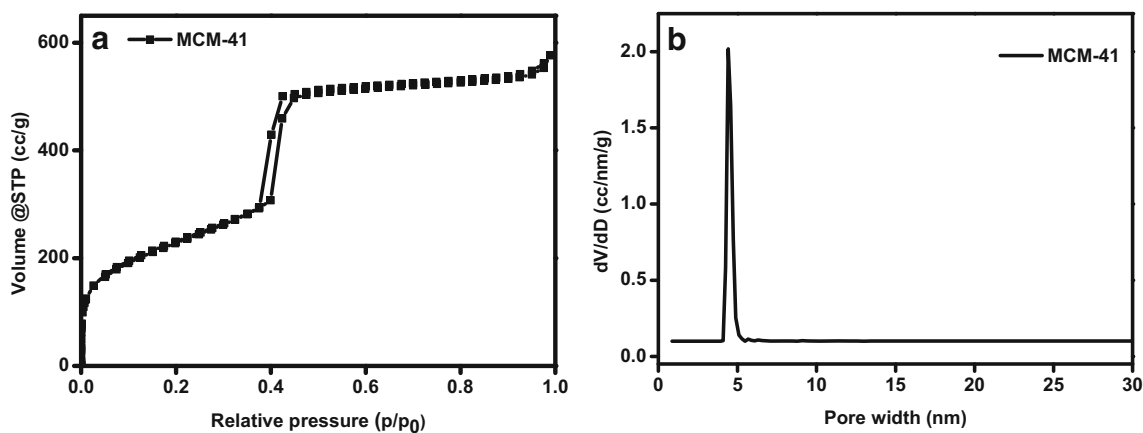


**Fig. 2** Gas analysis of MCM-41: **a** adsorption ( $N_2$  at 77 K) isotherm and **b** pore size distribution from NLDFT

nanopore size, and large specific surface area all seem to make our MCM-41 sample an advantageous model material for adsorption studies. Yet, when MCM-41 is in contact with water, potential influences of several factors such as the fraction of pore filling by water and dissolution of silica should be evaluated. We estimated the degree of nanopore filling by DSC measurements of MCM-41 sample immersed in sufficient water. As shown in Fig. 3, while

the normal melting temperature of the excessive water outside nanopores of MCM-41 was observed to be around  $0^\circ C$ , the drastic depression of freezing and melting temperatures of water inside nanopores (to  $-36.5$  and  $-32.1^\circ C$  respectively) clearly suggests the effect of nano-confinement mentioned earlier. More importantly, the degree of pore filling by water ( $\phi$ ) can be calculated using the following equations:

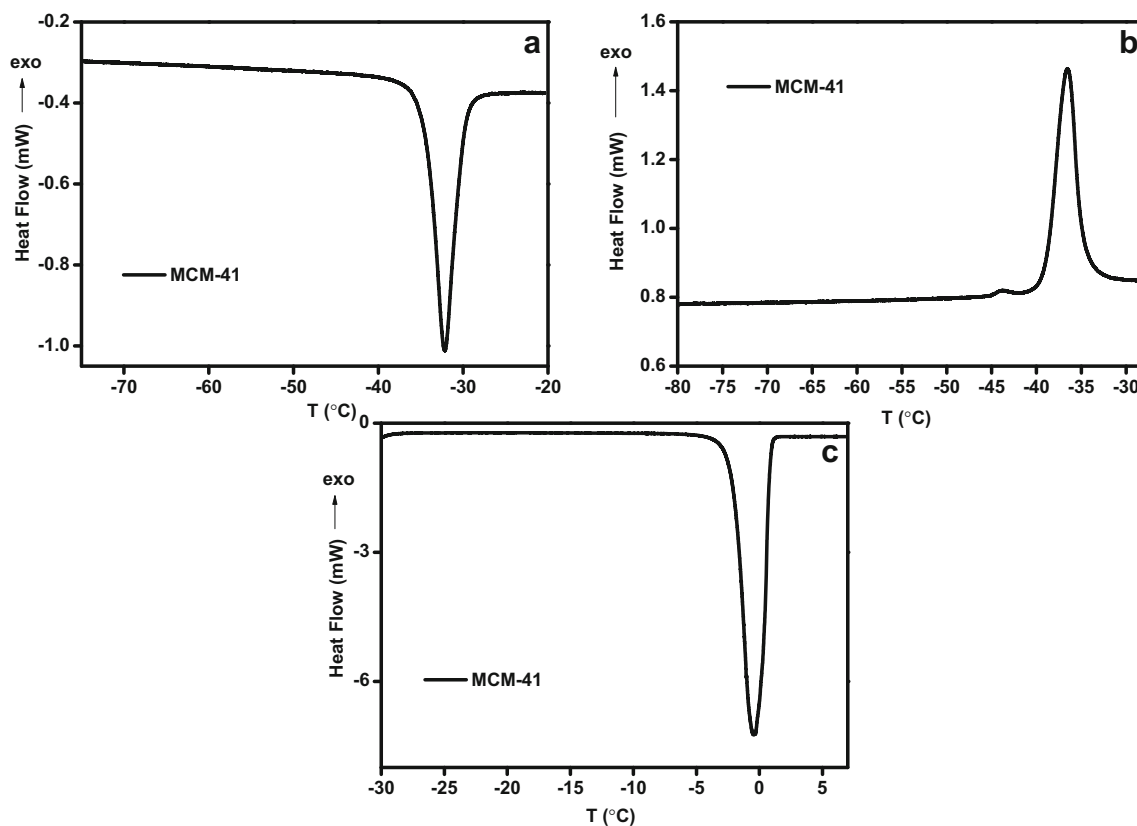


**Fig. 3** **a** DSC scanning curve, the freezing peaks of water inside the MCM-41 **b** DSC scanning curve, the melting peaks of ice inside the MCM-41 **c** DSC scanning curve, the melting peaks of water outside the MCM-41

$$m_{\text{inH}_2\text{O}} = m_{\text{H}_2\text{O}} - \frac{M_{\text{H}_2\text{O}} \times (m_{\text{MCM-41}} + m_{\text{H}_2\text{O}}) \times \Delta_{\text{ful}}H_{\text{out}}}{\Delta_{\text{ful}}H_{(\text{H}_2\text{O},\text{S})}} \quad (2)$$

$$V_{\text{inH}_2\text{O}} = m_{\text{inH}_2\text{O}} / \rho_{\text{H}_2\text{O}} \quad (3)$$

$$\varphi = V_{\text{inH}_2\text{O}} / V_{\text{nanopore}} \times 100\% \quad (4)$$

where  $m_{\text{inH}_2\text{O}}$  is the mass of water inside nanopores,  $m_{\text{outH}_2\text{O}}$  is the mass of water outside of nanopores,  $m_{\text{H}_2\text{O}}$  is the total mass of water added,  $\Delta_{\text{ful}}H_{\text{out}}$  is fusion heat of ice outside of nanopores,  $\Delta_{\text{ful}}H_{(\text{H}_2\text{O},\text{S})}$  is standard fusion heat of ice,  $V_{\text{nanopore}}$  is the pore volume and  $V_{\text{inH}_2\text{O}}$  is the volume of water inside of nanopores (see Table 1). The calculated degree of pore filling from repeated DSC measurements is always slightly larger than 100% suggesting complete and probably easy filling of MCM-41 nanopores, which further implies negligible effect of pore filling on the adsorption process (da Silva et al. 2009; Findenegg et al. 2008). Moreover, the structural stability of MCM-41 in water was checked by comparing the XRD patterns of samples before

and after being shaken in water (pH = 5, 25 °C) for 24 h. The negligible difference between the XRD patterns suggests that our MCM-41 sample is robust enough to survive significant structural degradation due to shaking or dissolution in water under our experimental condition of adsorption.

The PZC is considered an important property for adsorbents with charged surfaces. The PZC of MCM-41 was determined by following a previously reported method using an automatic potentiometric titrator (Huang and Stumm 1973). The acid-base titration data are plotted in Fig. 4, with the  $\text{pH}_{\text{apparent PZC}}$  value being estimated to be 2.9 (i.e., the pH value at the intersection point of the titration curves). Therefore, the surface charge of MCM-41 should be positive, around zero, or negative at pH lower than, equal to, or larger than 2.9, respectively.

**Table 1** Freezing, melting temperatures and  $\Delta_{\text{ful}}H$  of water in the MCM-41 silica

| Sample | $m_{\text{MCM-41}}$ (mg) | $m_{\text{H}_2\text{O}}$ (mg) | $T_f$ (°C) | $T_m$ (°C) | $\Delta_{\text{ful}}H_{\text{in}}$ (J/g) | $\Delta_{\text{ful}}H_{\text{out}}$ (J/g) |
|--------|--------------------------|-------------------------------|------------|------------|--|---|
| MCM-41 | 2.3                      | 7.8                           | - 36.5     | - 32.1     | 24.2                                     | 172.3                                     |

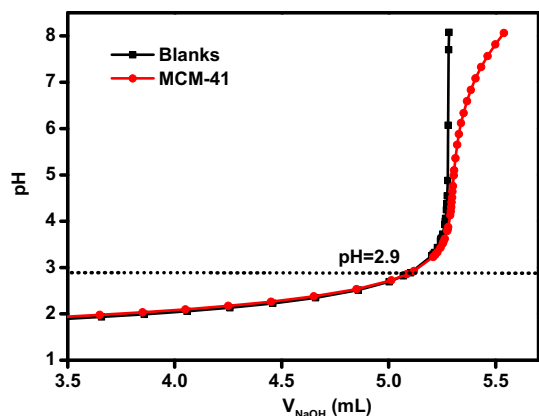


**Fig. 4** Schematic representation of the potentiometric titrations of a MCM-41 suspension (red line) and a blank solution (black line)

### 3.2 Effect of experimental conditions on adsorption

A variety of relevant adsorption parameters (such as pH, contact time, ionic strength, temperature) are expected to significantly influence the adsorption behavior of  $\text{Cu}^{2+}$  on MCM-41 nanoporous silica and were thus systematically investigated through batch experiments. The effect of time and temperature is presented in Fig. 5a. It can be seen that the amount of adsorption increases rapidly in the first several hours and then gradually with the prolongation of contact time until it reaches its maximum within 24 h. Whereas the initial rapid adsorption rate is normally attributed to the higher availability of metal ions ( $\text{Cu}^{2+}$ ) and functional groups on the silica adsorbent, the prolonged plateau in the adsorption curve probably implies the hindered diffusivity of  $\text{Cu}^{2+}$  inside the narrow nanopores. In the following experiments, the contact time was set as 24 h to obtain the adsorption capacity at equilibrium. The higher initial adsorption rate at 25 °C than that at 5 °C seems to reinforce the diffusion control on the adsorption kinetics. The equilibrium adsorption amount of  $\text{Cu}^{2+}$  was

0.29 mg/g at 25 °C, higher than that (0.22 mg/g) at 5 °C, which is interpreted as a consequence of an endothermic adsorption process (see Sect. 3.3).

The effect of pH on the equilibrium adsorption capacity of MCM-41 is shown in Fig. 5b. The adsorption capacity apparently follows an increasing trend with the increase of initial pH values from 3 to 5. Since the  $\text{pH}_{\text{apparent PZC}}$  value for MCM-41 was determined to be 2.9, the increasing pH also resulted in a greater extent of deprotonation of surface silanol groups and thus more negative charges on the MCM-41 surface. The similar influence of pH on both the adsorption capacity and the absolute surface charge density suggests that the electrostatic attraction between  $\text{Cu}^{2+}$  ions and  $\text{SiO}^-$  surface charges constitutes an important driving force of the adsorption process. Moreover, a slight decrease of the suspension pH was observed after the adsorption process, indicating certain ion exchange between  $\text{Cu}^{2+}$  and  $\text{H}^+$  from the surface silanols (Echeverria et al. 2003). At pH higher than 5, hydrolysis of  $\text{Cu}^{2+}$  ions and precipitation of  $\text{Cu}(\text{OH})_2$  may become serious, making such a condition inappropriate for adsorption studies (Stumm and Morgan 1996).

When the adsorption experiment was conducted in the presence of an often assumed “inert” electrolyte solution (i.e.,  $\text{NaNO}_3$ , 10 mg/L or 0.01 M), a pronounced decrease in the adsorption capacity of  $\text{Cu}^{2+}$  was observed from Fig. 6. A common reason to account for such a depressed adsorption capacity is that an increased ionic strength can lower the electric potential of the charged surface, compress the electric double layer (Kraepiel et al. 1998; Wang and Revil 2010), and thus weaken the electrostatic attraction between  $\text{Cu}^{2+}$  and charged MCM-41 surface. Another reason supported by the declined  $\text{Na}^+$  concentration in the solution is that  $\text{Na}^+$  and  $\text{Cu}^{2+}$  ions can actively compete for the adsorption sites on the MCM-41 surface. The existence of such a competitive role suggests that salts such as  $\text{NaNO}_3$  cannot simply be considered just an inert

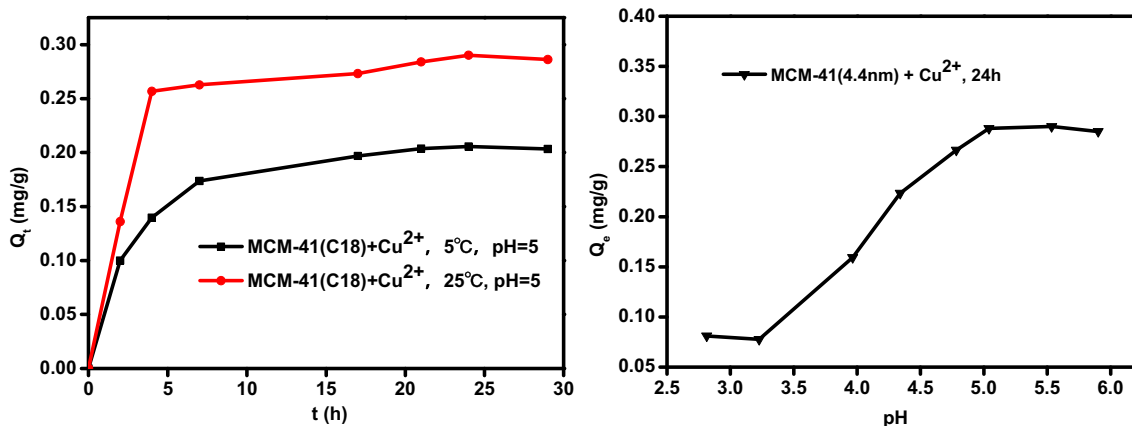


**Fig. 5** Effect of a adsorption time, temperature, and b pH on  $\text{Cu}^{2+}$  adsorption

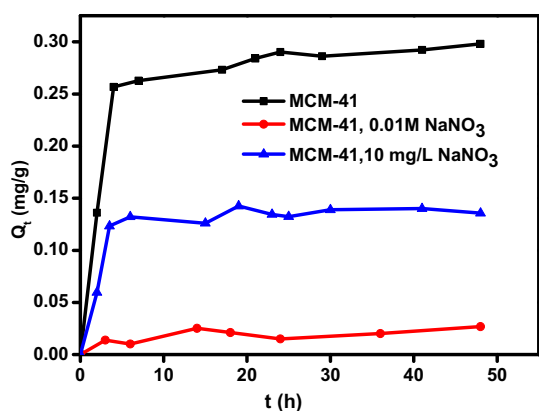


**Fig. 6** Effect of salt on the adsorption of  $\text{Cu}^{2+}$  on MCM-41

electrolyte when studying the adsorption of metal ions on nanoporous materials. More importantly, based on the perception that outer-sphere complexes (compared with inner-sphere complexes) are much more susceptible to the introduction of an electrolyte solution during adsorption (Baeyens and Bradbury 1997; Gao et al. 2015), it can be preliminarily inferred that at least a large proportion of adsorbed  $\text{Cu}^{2+}$  ions form outer-sphere complexes with MCM-41 nanoporous silica. This recognition perhaps highlights an important distinction between the adsorption of metal ions on nanoporous silica and that on nonporous silica, because formation of inner-sphere complexes has been substantiated on nonporous silica (Cheah et al. 1998, 2000).

### 3.3 Adsorption thermodynamics

Langmuir and Freundlich models are widely employed to fit adsorption data. Langmuir isotherm is based on localized monolayer adsorption at a set temperature. The Langmuir adsorption equation can be written in the following form:

$$Q_e = Q_m b C_e / (1 + b C_e) \quad (5)$$

where  $Q_e$  is the amount of solute adsorbed per unit weight of adsorbent at equilibrium (mg/g);  $C_e$  is the equilibrium bulk concentration of adsorbate (mg/L);  $Q_m$  is the maximum surface density at monolayer coverage (mg/g);  $b$  is the Langmuir constant (L/mg). Freundlich isotherm is an empirical formula to model multilayer adsorption on heterogeneous surfaces (Wu 2007), and is expressed as:

$$Q_e = K_f C_e^{(1/n)} \quad (6)$$

where  $Q_e$  and  $C_e$ , as defined above, are the equilibrium amount adsorbed (mg/g) and bulk equilibrium adsorptive concentration (mg/L), respectively.  $K_f$  is the Freundlich constant (mg/g) representing the strength of the adsorptive

bond, and  $n$  is a characteristic factor related to the bond distribution (Reed and Matsumoto 1993).

As shown in Fig. 7, our experimental data were fitted to the Langmuir and Freundlich models using the non-linear method. The model parameters of Langmuir and Freundlich isotherms are presented in Table 2. The  $R^2$  value of Langmuir isotherm appears close to that of Freundlich isotherm, making it inconspicuous to identify a better fit. As indicated by the effect of suspension pH on the adsorption capacity, adsorption of  $\text{Cu}^{2+}$  might go through monolayer binding of  $\text{Cu}^{2+}$  ions to the -OH groups on MCM-41 wall. It is also possible that  $\text{Cu}^{2+}$  can diffuse and fill in the MCM-41 nanopores through electrostatic attraction. If the adsorption capacity at equilibrium is converted to the ion volume concentration inside nanopores, an “enrichment factor” (i.e., the concentration ratio of ions inside and outside nanopores) can reach as high as 45, which manifests the dramatic effect of nanopores on ion distribution in relevant micro-environments.

Since the Freundlich model is purely empirical and lacks any solid theoretical basis, we used the Langmuir model to obtain thermodynamic parameters for the adsorption process. The Gibbs free energy change ( $\Delta G^\ominus$ ) is the fundamental criterion of spontaneity in adsorption systems. At a given temperature, adsorption reactions occur spontaneously if  $\Delta G^\ominus$  is a negative quantity. The Langmuir constant obtained from isotherm fitting is related to the adsorption  $\Delta G^\ominus$  and other thermodynamic parameters through the following equations (Sabio et al. 2001; Saeed and Ahmed 2006):

$$\Delta G^\ominus = -RT \ln(b\omega) \quad (7)$$

$$\ln b = -\Delta H^\ominus / (RT) + \Delta S^\ominus / R \quad (8)$$

$$\Delta G = \Delta H - T\Delta S \quad (9)$$

where  $\omega$  refers to the standard mass concentration of the solution.

The results of the thermodynamic calculation are shown in Table 2. It can be seen that the  $\Delta G^\ominus$  values are  $-18.39$  and  $-21.36$  kJ/mol at 278 and 298 K respectively, verifying that the sorption process was spontaneous. The decreasing value of  $\Delta G^\ominus$  with increasing temperature implies that the spontaneity degree increased as the temperature increased, consistent with our previous mentioned temperature effect. The positive  $\Delta H^\ominus$  value (22.75 kJ/mol) indicates that the adsorption process was endothermic, possibly involving breaking the ion-water and water-water bonding of hydrated metal ions (Saeed and Ahmed 2006). The positive  $\Delta S^\ominus$  value (148 J/mol) suggests increasing randomness during the adsorption of metal ions on MCM-41, possibly resulting from the dehydration of the bound water molecules. Therefore, the adsorption of  $\text{Cu}^{2+}$  on

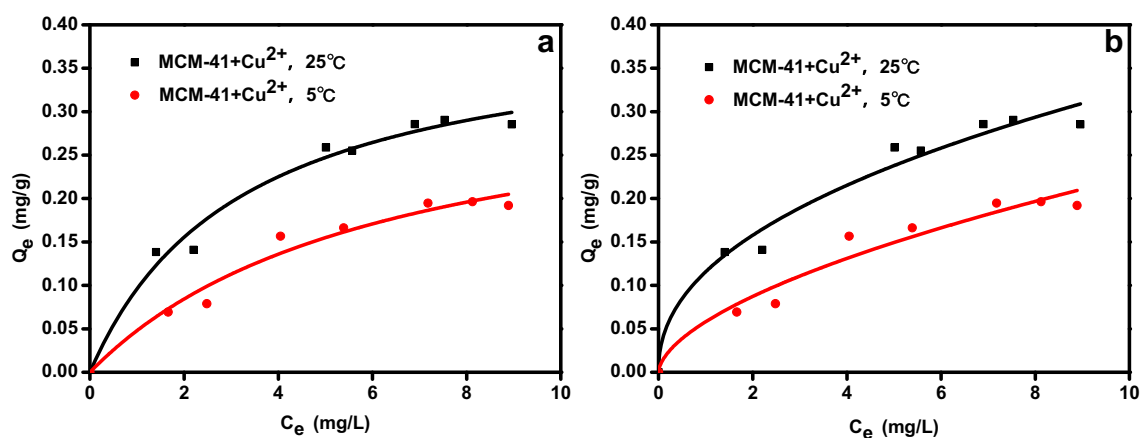


**Fig. 7** Fitting of adsorption isotherms through **a** Langmuir and **b** Freundlich models

**Table 2** Fitting parameters of Langmuir and Freundlich models determined by non-linear method, and thermodynamic parameters derived from Langmuir model ( $\Delta G$ : kJ/mol;  $\Delta H$ : kJ/mol;  $\Delta S$ : J/mol)

| SampleID | T (K) | Exp. $Q_e$ | Freundlich $Q_e = K_f C_e^{(1/n)}$ |        |        | Langmuir $Q_e = Q_m b C_e / (1 + b C_e)$ |        |        | Thermodynamic Parameters |            |            |
|----------|-------|------------|------------------------------------|--------|--------|--|--------|--------|--------------------------|------------|------------|
|          |       |            | N                                  | $K_f$  | $R^2$  | $Q_m$                                    | b      | $R^2$  | $\Delta G$               | $\Delta H$ | $\Delta S$ |
| MCM-41   | 278   | 0.22       | 1.7059                             | 0.0581 | 0.9502 | 0.3501                                   | 0.1586 | 0.9670 | - 18.39                  | 22.75      | 148        |
| MCM-41   | 298   | 0.29       | 2.1750                             | 0.1088 | 0.9755 | 0.3971                                   | 0.2955 | 0.9674 | - 21.36                  | 22.75      | 148        |

MCM-41 nanoporous silica is considered an entropy-driven, endothermic, spontaneous process.

### 3.4 Adsorption kinetics

The kinetics of any adsorption process can be influenced by the structure of adsorbent, properties and concentrations of adsorbate, and interaction between adsorbent and adsorbate (Kyriakopoulos and Douliua 2006; Mohan and Singh 2002). The linear fitting method was used to fit our kinetic data with two well-known kinetic models as shown below:

$$\ln(Q_e - Q_t) = \ln Q_e - k_1 t \quad \text{Pseudo - first - order model} \quad (10)$$

$$t/Q_t = (1/k_2 Q_e^2) + (1/Q_e)t \quad \text{Pseudo - second - order model} \quad (11)$$

where  $Q_e$  is amount adsorbed at equilibrium,  $Q_t$  is amount adsorbed at time  $t$ ,  $k_1$  and  $k_2$  are the pseudo-first-order and pseudo-second-order rate constants of adsorption, respectively. It is clear that our data fit better with the pseudo-second-order equation, as evident from the much higher  $R^2$  value (see Fig. 8). This fitting result also implies that the adsorption process might involve interaction between  $\text{Cu}^{2+}$  and silanol groups on MCM-41 silica.

In mechanism study of adsorption, characteristics of adsorbate and adsorbent, and their interaction through the contact time are generally considered. The adsorption mechanism may become much more complicated when it involves nanoporous materials with pore diffusion playing an important role. The adsorption of the metal ion by porous adsorbents usually has three main steps:

1. The migration of adsorbate to the outer surface of adsorbent (film-diffusion).
2. The migration of adsorbate in the pores of adsorbent (intra-particle diffusion).
3. Adsorption of adsorbate in porous adsorbents.

Obviously, the slowest transport step would determine the total adsorption rate (Sen Gupta and Bhattacharyya 2011).

The Weber and Boyd model is usually used to study the diffusion mechanism because it determines the rate of ion diffusion in pores. Weber's diffusion model is represented by:

$$Q_t = k_d t^{1/2} \quad (12)$$

where  $Q_t$  is amount adsorbed at time  $t$ , and  $k_d$  ( $\text{mg}/(\text{gh}^{1/2})$ ) is the intra-particle diffusion rate constant. Applying The Weber and Morris model can help determine the rate-controlling mechanism of the adsorption process. The  $k_d$



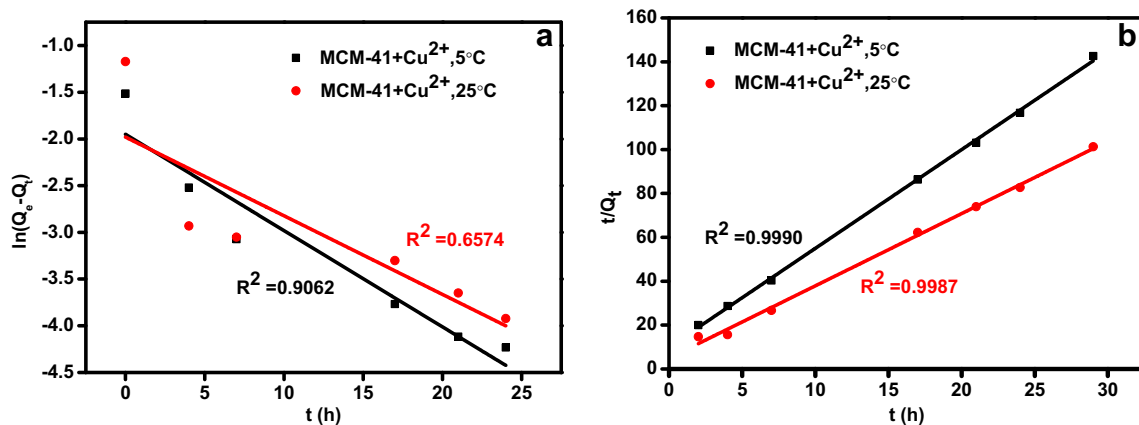


**Fig. 8** Kinetic analysis of Cu<sup>2+</sup> adsorption according to **a** pseudo-first-order model, and **b** pseudo-second-order model

value of MCM-41 is calculated to be 0.180 mg/(gh<sup>1/2</sup>). However, the plot in Fig. 9a does not pass through the origin, indicating that the intra-particle diffusion is not the only rate-controlling step (Acharya et al. 2009).

Boyd film-diffusion model assumes that the main resistance of diffusion is in the boundary layer around the adsorbed particles, and is expressed as:

$$F(t) = 1 - \left(\frac{6}{\pi^2}\right) \exp(-Bt) \tag{13}$$

$$F(t) = \frac{Q_t}{Q_e} \tag{14}$$

The equation below is obtained by taking the natural logarithm of the rearranged Eq. (13):

$$Bt = -0.4977 - \ln(1 - F(t)) \tag{15}$$

$$B = \frac{D_i \pi^2}{r^2} \tag{16}$$

where F(t) is the fraction of Cu<sup>2+</sup> adsorbed at different time, B can be used to calculate the effective diffusion coefficient D<sub>i</sub> (m<sup>2</sup>/h), r is the radius of the adsorbent

particles assuming a spherical shape. Boyd model analysis is presented in Fig. 9b. The plot of Bt against time t is linear but does not pass through the origin, implying film-diffusion control of the adsorption rate (Malash and El-Khaiary 2010). The D<sub>i</sub> value is found to be 1.3 × 10<sup>-14</sup> m<sup>2</sup>/h for MCM-41 nanoporous silica.

### 3.5 Spectral analysis of adsorption mechanism

In order to investigate the adsorption mechanism of Cu<sup>2+</sup> on MCM-41, ATR-IR measurement of MCM-41 samples before and after Cu<sup>2+</sup> adsorption was carried out. As shown in Fig. 10a, the absorption bands at around 1082, 970, and 800 cm<sup>-1</sup> are typical of silica species. Specifically, the bands at 1082 and 800 cm<sup>-1</sup> represent asymmetric and symmetric stretching vibrations of Si-O-Si, respectively. The band at 970 cm<sup>-1</sup> is ascribed to the stretching vibration of Si-OH species (Spiekermann et al. 2012). The asymmetry of the peak at around 970 cm<sup>-1</sup> indicates the presence of multiple vibrations, probably due to Si-O<sup>-</sup> and Si-OH groups for sample before Cu<sup>2+</sup>

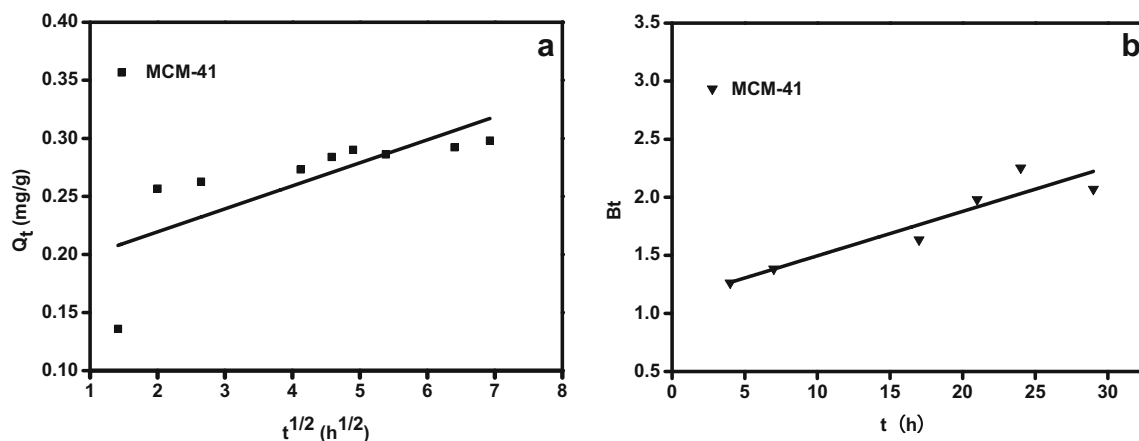


**Fig. 9** Diffusion kinetics analysis of Cu<sup>2+</sup> adsorption according to **a** Weber and Morris and **b** Boyd model

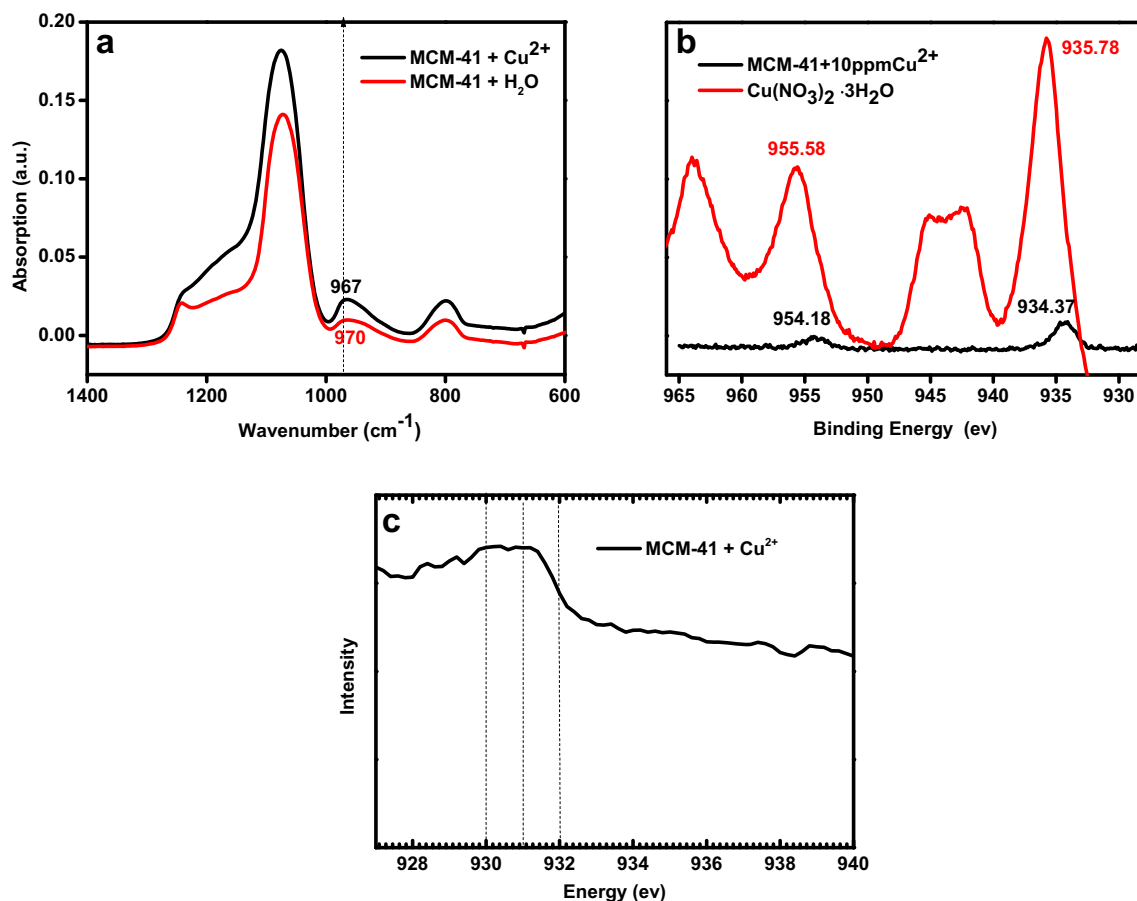


**Fig. 10** Spectral analysis of  $\text{Cu}^{2+}$  adsorption on MCM-41 **a** ATR-IR, **b** XPS, and **c** Cu  $L_3$ -edge XANES

adsorption (Ma et al. 2013). Compared with the peak at  $970\text{ cm}^{-1}$ , the slight red-shift to  $967\text{ cm}^{-1}$  for sample after  $\text{Cu}^{2+}$  adsorption is likely due to the intensity changes of several superimposing modes (including Si-O $^-$ , Si-OH and Si-O-Cu groups), suggesting a possible interaction between  $\text{Cu}^{2+}$  ions and Si-OH/Si-O $^-$  groups (Ma et al. 2013).

The Cu 2p XPS spectrum of the MCM-41 adsorbent after adsorption (initial  $\text{Cu}^{2+}$  concentration 10 mg/L, 24 h) is shown in Fig. 10b. The two peaks centered at 934.37 and 954.18 eV are attributed to the Cu  $2p_{3/2}$  and Cu  $2p_{1/2}$  levels of the  $\text{Cu}^{2+}$  species, respectively. Compared with that of  $\text{Cu}(\text{NO}_3)_2 \cdot 3\text{H}_2\text{O}$ , the Cu 2p XPS spectrum of MCM-41 after  $\text{Cu}^{2+}$  adsorption shifted to a lower energy level. This result again suggests the interaction between  $\text{Cu}^{2+}$  and the Si-OH, which leads to increased electron cloud density on copper ions and therefore lowered binding energy level of the adsorbed  $\text{Cu}^{2+}$  species (Ma et al. 2013; Yuan et al. 2013).

Figure 10c shows the Cu  $L_3$  XANES spectrum of MCM-41 after  $\text{Cu}^{2+}$  adsorption. The peak is assigned to the transition from the  $2p_{3/2}$  to the highest unoccupied 3d state. The XANES spectrum exhibits absorption maxima at 930.1 and 930.8 eV, which are assigned to  $\text{CuO}_4$  tetrahedra

and  $\text{CuO}_6$  octahedra respectively (Shimizu et al. 2000, 2001). This result implies that the  $\text{Cu}^{2+}$  adsorption process is probably accompanied by the formation of Si-O-Cu bonds, which seems to favor inner-sphere adsorption complexation consistent with previous investigations (Cheah et al. 1998; Nelson et al. 2017).

## 4 Conclusions

MCM-41 material with a uniform pore size (4.4 nm) and a large specific area ( $839\text{ m}^2/\text{g}$ ) was synthesized and used as a model adsorbent to systematically study the adsorption behavior of  $\text{Cu}^{2+}$  on nanoporous silica. The easy accessibility of the nanopores by aqueous solution as revealed by the high pore-filling degree ( $\sim 100\%$ ) serves as a solid foundation to validate the practical role of nanoporous media in numerous geological environments. A high value (over 45) of the dimensionless partition coefficient highlights the intense metal ion-enriching effect due to the existence of nanopores. The relatively slow adsorption kinetics is interpreted as a result of film diffusion and intra-particle diffusion associated with the restricted nanopores.

The adsorption capacity of  $\text{Cu}^{2+}$  decreases with the decrease of pH or the increase of ionic strength, suggesting the important role of electrostatic interaction between oppositely charged species. Thermodynamic analysis indicates that  $\text{Cu}^{2+}$  adsorption on nanoporous silica is a spontaneous entropy-driven process very likely involving an endothermal dehydration step. The often considered inert electrolyte (e.g.,  $\text{NaNO}_3$ ) significantly reduces the adsorption capacity through not only suppression of the electric double layer but also competition for the adsorbing sites, implying that a large proportion of adsorbed  $\text{Cu}^{2+}$  inside nanopores may engage in outer-sphere complexation. Conversely, spectroscopic characterization appears to support the formation of inner-sphere complexes. We believe that the severe superposition of electric potentials from the charged walls of narrow nanopores must constitute a key mechanism in the adsorption process, which certainly strengthens the electrostatic interaction and perhaps exerts substantial perturbation on the electronic structure of  $\text{Cu}^{2+}$  species.

**Acknowledgements** Financial supports from Natural Science Foundation of China (Grant No. 41473064/41603065) and Science Technology Department Foundation of Guizhou Province (Grant No. QianKeHe J [2015]2125) are greatly appreciated.

## References

- Acharya J, Sahu JN, Mohanty CR, Meikap BC (2009) Removal of lead(II) from wastewater by activated carbon developed from Tamarind wood by zinc chloride activation. *Chem Eng J* 149:249–262. <https://doi.org/10.1016/j.cej.2008.10.029>
- Baeyens B, Bradbury MH (1997) A mechanistic description of Ni and Zn sorption on Na-montmorillonite.1. Titration and sorption measurements. *J Contam Hydrol* 27:199–222. [https://doi.org/10.1016/s0169-7722\(97\)00008-9](https://doi.org/10.1016/s0169-7722(97)00008-9)
- Beck JS et al (1992) A new family of mesoporous molecular-sieves prepared with liquid-crystal templates. *J Am Chem Soc* 114:10834–10843. <https://doi.org/10.1021/ja00053a020>
- Ben Said I, Sadouki K, Masse S, Coradin T, Smiri LS, Fessi S (2018) Advanced Pd/CeZr(1-x)O2/MCM-41 catalysts for methane combustion: effect of the zirconium and cerium loadings. *Microporous Mesoporous Mat* 260:93–101. <https://doi.org/10.1016/j.micromeso.2016.10.044>
- Bernard S, Wirth R, Schreiber A, Schulz HM, Horsfield B (2012) Formation of nanoporous pyrobitumen residues during maturation of the Barnett Shale (Fort Worth Basin). *Int J Coal Geol* 103:3–11. <https://doi.org/10.1016/j.coal.2012.04.010>
- Bradl HB (2004) Adsorption of heavy metal ions on soils and soils constituents. *J Colloid Interface Sci* 277:1–18. <https://doi.org/10.1016/j.jcis.2004.04.005>
- Cheah SF, Brown GE, Parks GA (1998) XAFS spectroscopy study of Cu(II) sorption on amorphous  $\text{SiO}_2$  and gamma- $\text{Al}_2\text{O}_3$ : effect of substrate and time on sorption complexes. *J Colloid Interface Sci* 208:110–128. <https://doi.org/10.1006/jcis.1998.5678>
- Cheah SF, Brown GE, Parks GA (2000) XAFS study of Cu model compounds and  $\text{Cu}^{2+}$  sorption products on amorphous  $\text{SiO}_2$ , gamma- $\text{Al}_2\text{O}_3$ , and anatase. *Am Miner* 85:118–132. <https://doi.org/10.2138/am-2000-0113>
- Chen HY, Ding J, Wang WL, Wei XL, Lu JL (2017) Water adsorption characteristics of MCM-41 post-modified by Al grafting and cations doping: equilibrium and kinetics study. *Adsorpt. J Int Adsorpt Soc* 23:113–120. <https://doi.org/10.1007/s10450-016-9829-2>
- Cheng HF, Hu ED, Hu YA (2012) Impact of mineral micropores on transport and fate of organic contaminants: a review. *J Contam Hydrol* 129:80–90. <https://doi.org/10.1016/j.jconhyd.2011.09.008>
- Costa CC, Melo DMA, Melo MAF, Mendoza ME, Nascimento JC, Andrade JM, Barros JMF (2014) Effects of different structure-directing agents (SDA) in MCM-41 on the adsorption of  $\text{CO}_2$ . *J Porous Mat* 21:1069–1077. <https://doi.org/10.1007/s10934-014-9857-9>
- da Silva LCC et al (2009) DSC estimation of structural and textural parameters of SBA-15 silica using water probe. *J Therm Anal Calorim* 97:701–704. <https://doi.org/10.1007/s10973-009-0334-7>
- Dou BJ, Hu Q, Li JJ, Qiao SZ, Hao ZP (2011) Adsorption performance of VOCs in ordered mesoporous silicas with different pore structures and surface chemistry. *J Hazard Mater* 186:1615–1624. <https://doi.org/10.1016/j.jhazmat.2010.12.051>
- Echeverria J, Indurain J, Churio E, Garrido J (2003) Simultaneous effect of pH, temperature, ionic strength, and initial concentration on the retention of Ni on illite. *Colloids Surfaces Physicochem Eng Asp* 218:175–187. [https://doi.org/10.1016/s0927-7757\(02\)00587-3](https://doi.org/10.1016/s0927-7757(02)00587-3)
- Elo O, Müller K, Ikeda-Ohno A, Bok F, Scheinost AC, Hölttä P, Huittinen N (2017) Batch sorption and spectroscopic speciation studies of neptunium uptake by montmorillonite and corundum. *Geochim Cosmochim Acta* 198:168–181. <https://doi.org/10.1016/j.gca.2016.10.040>
- Faghihian H, Naghavi M (2014) Synthesis of amine-functionalized MCM-41 and MCM-48 for removal of heavy metal ions from aqueous solutions. *Sep Sci Technol* 49:214–220. <https://doi.org/10.1080/01496395.2013.819516>
- Findenegg GH, Jahnert S, Akcakayiran D, Schreiber A (2008) Freezing and melting of water confined in silica nanopores. *ChemPhysChem* 9:2651–2659. <https://doi.org/10.1002/cphc.200800616>
- Gao Y, Shao ZY, Xiao ZH (2015) U(VI) sorption on illite: effect of pH, ionic strength, humic acid and temperature. *J Radioanal Nucl Chem* 303:867–876. <https://doi.org/10.1007/s10967-014-3385-6>
- Gibson LT (2014) Mesosilica materials and organic pollutant adsorption: part A removal from air. *Chem Soc Rev* 43:5163–5172. <https://doi.org/10.1039/c3cs60096c>
- Grun M, Unger KK, Matsumoto A, Tsutsumi K (1999) Novel pathways for the preparation of mesoporous MCM-41 materials: control of porosity and morphology. *Microporous Mesoporous Mat* 27:207–216. [https://doi.org/10.1016/s1387-1811\(98\)00255-8](https://doi.org/10.1016/s1387-1811(98)00255-8)
- Gu YT, Wan Q, Yu WB, Li XX, Yu ZB (2018) The effects of clay minerals and organic matter on nanoscale pores in Lower Paleozoic shale gas reservoirs, Guizhou. *China Acta Geochimica* 37:791–804
- Guo K et al (2015) Adsorption of Cs from water on surface-modified MCM-41 mesosilicate. *Water Air Soil Pollut* 226:9. <https://doi.org/10.1007/s11270-015-2565-5>
- He R et al (2018) Design and fabrication of highly ordered ion imprinted SBA-15 and MCM-41 mesoporous organosilicas for efficient removal of  $\text{Ni}^{2+}$  from different properties of wastewaters. *Microporous Mesoporous Mater* 257:212–221. <https://doi.org/10.1016/j.micromeso.2017.08.007>

- Hochella MF (2013) Standing back and looking at the forest: a perspective on surfaces and interfaces, the ubiquitous stuff of nearly all things. *Elements* 9:171–172
- Hochella MF, Banfield JF (1995) Chemical weathering of silicates in nature: a microscopic perspective with theoretical considerations. *Chem Weather Rates Silicate Miner* 31:353–406
- Hochella MF, Lower SK, Maurice PA, Penn RL, Sahai N, Sparks DL, Twining BS (2008) Nanominerals, mineral nanoparticles, and earth systems. *Science* 319:1631–1635. <https://doi.org/10.1126/science.1141134>
- Hu YL, Wang HB, Chen ZW, Li XG (2018) Titanium incorporated mesoporous silica immobilized functional ionic liquid as an efficient reusable catalyst for cycloaddition of carbon dioxide to epoxides. *ChemistrySelect* 3:5087–5091. <https://doi.org/10.1002/slct.201800984>
- Huang CP, Stumm W (1973) Specific adsorption of cations on hydrous gamma-Al<sub>2</sub>O<sub>3</sub>. *J Colloid Interface Sci* 43:409–420. [https://doi.org/10.1016/0021-9797\(73\)90387-1](https://doi.org/10.1016/0021-9797(73)90387-1)
- Huang J, Ye M, Qu YQ, Chu LF, Chen R, He QZ, Xu DF (2012) Pb (II) removal from aqueous media by EDTA-modified mesoporous silica SBA-15. *J Colloid Interface Sci* 385:137–146. <https://doi.org/10.1016/j.jcis.2012.06.054>
- Huo QS, Margolese DI, Stucky GD (1996) Surfactant control of phases in the synthesis of mesoporous silica-based materials. *Chem Mat* 8:1147–1160. <https://doi.org/10.1021/cm960137h>
- Jahnert S, Chavez FV, Schaumann GE, Schreiber A, Schonhoff M, Findenegg GH (2008) Melting and freezing of water in cylindrical silica nanopores. *Phys Chem Chem Phys* 10:6039–6051. <https://doi.org/10.1039/b809438c>
- Knight AW, Tigges AB, Ilgen AG (2018) Adsorption of copper (II) on mesoporous silica: the effect of nano-scale confinement. *Geochem Trans* 19:13. <https://doi.org/10.1186/s12932-018-0057-4>
- Kraepiel AML, Keller K, Morel FMM (1998) Morel FMM (1999) On the acid-base chemistry of permanently charged minerals (vol 32, pg 2829. *Environ Sci Technol* 33:516. <https://doi.org/10.1021/es9820184>
- Kruk M, Jaroniec M, Sayari A (1997) Adsorption study of surface and structural properties of MCM-41 materials of different pore sizes. *J Phys Chem B* 101:583–589. <https://doi.org/10.1021/jp962000k>
- Kyriakopoulos GL, Doulia D (2006) Adsorption of pesticides on carbonaceous and polymeric materials from aqueous solutions: a review. *Sep Purif Rev* 35:97–191. <https://doi.org/10.1080/15422110600822733>
- Lam KF, Yeung KL, McKay G (2007) Selective mesoporous adsorbents for Cr(2)O<sub>2</sub>/7-and Cu<sup>2+</sup> separation. *Microporous Mesoporous Mater* 100:191–201. <https://doi.org/10.1016/j.micro-meso.2006.10.037>
- Lee JY, Chen CH, Cheng S, Li HY (2016) Adsorption of Pb(II) and Cu(II) metal ions on functionalized large-pore mesoporous silica. *Int J Environ Sci Technol* 13:65–76. <https://doi.org/10.1007/s13762-015-0841-y>
- Loucks RG, Reed RM, Ruppel SC, Jarvie DM (2009) Morphology genesis, and distribution of nanometer-scale pores in siliceous mudstones of the mississippian barnett shale. *J Sediment Res* 79:848–861. <https://doi.org/10.2110/jsr.2009.092>
- Ma XB et al (2013) Hydrogenation of dimethyl oxalate to ethylene glycol over mesoporous Cu-MCM-41 catalysts. *Aiche J* 59:2530–2539. <https://doi.org/10.1002/aic.13998>
- Malash GF, El-Khaiary MI (2010) Piecewise linear regression: a statistical method for the analysis of experimental adsorption data by the intraparticle-diffusion models. *Chem Eng J* 163:256–263. <https://doi.org/10.1016/j.cej.2010.07.059>
- Matsumoto A, Tsutsumi K, Schumacher K, Unger KK (2002) Surface functionalization and stabilization of mesoporous silica spheres by silanization and their adsorption characteristics. *Langmuir* 18:4014–4019. <https://doi.org/10.1021/la020004c>
- Mohan D, Singh KP (2002) Single- and multi-component adsorption of cadmium and zinc using activated carbon derived from bagasse—an agricultural waste. *Water Res* 36:2304–2318. [https://doi.org/10.1016/s0043-1354\(01\)00447-x](https://doi.org/10.1016/s0043-1354(01)00447-x)
- Nelson J, Wasylenki L, Bargar JR, Brown GE, Maher K (2017) Effects of surface structural disorder and surface coverage on isotopic fractionation during Zn(II) adsorption onto quartz and amorphous silica surfaces. *Geochim Cosmochim Acta* 215:354–376. <https://doi.org/10.1016/j.gca.2017.08.003>
- Oliver S, Kuperman A, Coombs N, Lough A, Ozin GA (1995) Lamellar aluminophosphates with surface patterns that mimic diatom and radiolarian microskeletons. *Nature* 378:47–50. <https://doi.org/10.1038/378047a0>
- Radha B et al (2016) Molecular transport through capillaries made with atomic-scale precision. *Nature* 538:222–225. <https://doi.org/10.1038/nature19363>
- Ravi S, Roshan R, Tharun J, Park DW, Chun HH, Park H, Selvaraj M (2015) Mesoporous silica-giant particle with slit pore arrangement as an adsorbent for heavy metal oxyanions from aqueous medium *RSC Adv* 5:10260–10266. <https://doi.org/10.1039/c4ra12175a>
- Reed BE, Matsumoto MR (1993) Modeling cadmium adsorption by activated carbon using the Langmuir and Freundlich isotherm expressions. *Sep Sci Technol* 28(13–14):2179–2195. <https://doi.org/10.1080/01496399308016742>
- Rother G, Krukowski EG, Wallacher D, Grimm N, Bodnar RJ, Cole DR (2012) Pore size effects on the sorption of supercritical CO<sub>2</sub> in Mesoporous CPG-10 Silica. *J Phys Chem C* 116:917–922. <https://doi.org/10.1021/jp209341q>
- Sabio E, Gonzalez-Martin ML, Ramiro A, Gonzalez JF, Bruque JM, Labajos-Broncano L, Encinar JM (2001) Influence of the regeneration temperature on the phenols adsorption on activated carbon. *J Colloid Interface Sci* 242:31–35. <https://doi.org/10.1006/jcis.2001.7775>
- Saeed MM, Ahmed M (2006) Effect of temperature on kinetics and adsorption profile of endothermic chemisorption process—Tm(III)-PAN loaded PUF system. *Sep Sci Technol* 41:705–722. <https://doi.org/10.1080/01496390500527993>
- Schreiber A, Ketelsen I, Findenegg GH (2001) Melting and freezing of water in ordered mesoporous silica materials. *Phys Chem Chem Phys* 3:1185–1195. <https://doi.org/10.1039/b010086m>
- Schulthess CP, Taylor RW, Ferreira DR (2011) The nanopore inner sphere enhancement effect on cation adsorption: sodium and nickel. *Soil Sci Soc Am J* 75:378–388. <https://doi.org/10.2136/sssaj2010.0129nps>
- Sen Gupta S, Bhattacharyya KG (2011) Kinetics of adsorption of metal ions on inorganic materials: a review. *Adv Coll Interface Sci* 162:39–58. <https://doi.org/10.1016/j.cis.2010.12.004>
- Senapati S, Chandra A (2001) Dielectric constant of water confined in a nanocavity. *J Phys Chem B* 105:5106–5109. <https://doi.org/10.1021/jp011058i>
- Shimizu K, Maeshima H, Yoshida H, Satsuma A, Hattori T (2000) Spectroscopic characterisation of Cu-Al<sub>2</sub>O<sub>3</sub> catalysts for selective catalytic reduction of NO with propene. *Phys Chem Chem Phys* 2:2435–2439. <https://doi.org/10.1039/b000943i>
- Shimizu K, Maeshima H, Yoshida H, Satsuma A, Hattori T (2001) Ligand field effect on the chemical shift in XANES spectra of Cu(II) compounds. *Phys Chem Chem Phys* 3:862–866. <https://doi.org/10.1039/b007276l>
- Singer DM, Guo H, Davis JA (2014) U(VI) and Sr(II) batch sorption and diffusion kinetics into mesoporous silica (MCM-41). *Chem Geol* 390:152–163. <https://doi.org/10.1016/j.chemgeo.2014.10.027>

- Spiekermann G, Steele-MacInnis M, Schmidt C, Jahn S (2012) Vibrational mode frequencies of silica species in SiO<sub>2</sub>-H<sub>2</sub>O liquids and glasses from ab initio molecular dynamics. *J Chem Phys* 136:13. <https://doi.org/10.1063/1.3703667>
- Stumm W, Morgan JJ (1996) *Aquatic chemistry; an introduction emphasizing chemical equilibria in natural waters*, 3rd edn. Wiley, Hoboken
- Taguchi A, Schuth F (2005) Ordered mesoporous materials in catalysis. *Microporous Mesoporous Mater* 77:1–45. <https://doi.org/10.1016/j.micromeso.2004.06.030>
- Takei T, Mukasa K, Kofuji M, Fuji M, Watanabe T, Chikazawa M, Kanazawa T (2000) Changes in density and surface tension of water in silica pores. *Colloid Polym Sci* 278:475–480. <https://doi.org/10.1007/s003960050542>
- Thirumavalavan M, Wang YT, Lin LC, Lee JF (2011) Monitoring of the structure of mesoporous silica materials tailored using different organic templates and their effect on the adsorption of heavy metal ions. *J Phys Chem C* 115:8165–8174. <https://doi.org/10.1021/jp200029g>
- Thommes M, Kaneko K, Neimark AV, Olivier JP, Rodriguez-Reinoso F, Rouquerol J, Sing KSW (2015) Physisorption of gases, with special reference to the evaluation of surface area and pore size distribution (IUPAC Technical Report) *Pure Appl Chem* 87(9–10):1051–1069. <https://doi.org/10.1515/pac-2014-1117>
- Tian L, Xie G, Li RX, Yu XH, Hou YQ (2011) Removal of Cr (VI) from aqueous solution using MCM-41. *Desalin Water Treat* 36:334–343. <https://doi.org/10.5004/dwt.2011.2521>
- Wang M, Revil A (2010) Electrochemical charge of silica surfaces at high ionic strength in narrow channels. *J Colloid Interface Sci* 343:381–386. <https://doi.org/10.1016/j.jcis.2009.11.039>
- Wang YF, Bryan C, Xu HF, Pohl P, Yang Y, Brinker CJ (2002) Interface chemistry of nanostructured materials: ion adsorption on mesoporous alumina. *J Colloid Interface Sci* 254:23–30. <https://doi.org/10.1006/jcis.2002.8571>
- Wang YF, Bryan C, Xu HF, Gao HZ (2003) Nanogeochemistry: geochemical reactions and mass transfers in nanopores. *Geology* 31:387–390. [https://doi.org/10.1130/0091-7613\(2003\)031%3c0387:ngramt%3e2.0.co;2](https://doi.org/10.1130/0091-7613(2003)031%3c0387:ngramt%3e2.0.co;2)
- Wu CH (2007) Studies of the equilibrium and thermodynamics of the adsorption of Cu<sup>2+</sup> onto as-produced and modified carbon nanotubes. *J Colloid Interface Sci* 311:338–346. <https://doi.org/10.1016/j.jcis.2007.02.077>
- Wu D, Navrotsky A (2013) Small molecule—silica interactions in porous silica structures. *Geochim Cosmochim Acta* 109:38–50. <https://doi.org/10.1016/j.gca.2013.01.038>
- Wu D, Hwang SJ, Zones SI, Navrotsky A (2014) Guest-host interactions of a rigid organic molecule in porous silica frameworks. *Proc Natl Acad Sci USA* 111:1720–1725. <https://doi.org/10.1073/pnas.1323989111>
- Xu X, Tian BZ, Kong JL, Zhang S, Liu BH, Zhao DY (2003) Ordered mesoporous niobium oxide film: a novel matrix for assembling functional proteins for bioelectrochemical applications. *Adv Mater* 15:1932. <https://doi.org/10.1002/adma.200305424>
- Yuan P, Southon PD, Liu ZW, Green MER, Hook JM, Antill SJ, Kepert CJ (2008) Functionalization of halloysite clay nanotubes by grafting with gamma-aminopropyltriethoxysilane. *J Phys Chem C* 112:15742–15751. <https://doi.org/10.1021/jp805657t>
- Yuan P et al (2013) Surface silylation of mesoporous/macroporous diatomite (diatomaceous earth) and its function in Cu(II) adsorption: the effects of heating pretreatment. *Microporous Mesoporous Mater* 170:9–19. <https://doi.org/10.1016/j.micro-meso.2012.11.030>
- Zhang QD, Liu N, Cao YZ, Zhang WF, Wei Y, Feng L, Jiang L (2018) A facile method to prepare dual-functional membrane for efficient oil removal and in situ reversible mercury ions adsorption from wastewater. *Appl Surf Sci* 434:57–62. <https://doi.org/10.1016/j.apsusc.2017.09.230>
- Zimmerman AR, Chorover J, Goyne KW, Brantley SL (2004) Protection of mesopore-adsorbed organic matter from enzymatic degradation. *Environ Sci Technol* 38:4542–4548. <https://doi.org/10.1021/es035340+>